

SCIENTIFIC REPORTS



OPEN

Unveiling high specific energy supercapacitor from layer-by-layer assembled polypyrrole/graphene oxide|polypyrrole/manganese oxide electrode material

Shalini Kulandaivalu¹, Nadhrah Suhaimi¹ & Yusran Sulaiman ^{1,2}

A novel layer-by-layer (LBL) based electrode material for supercapacitor consists of polypyrrole/graphene oxide and polypyrrole/manganese oxide (PPy|GO|PPy/MnO₂) has prepared by electrochemical deposition. The formation of LBL assembled nanocomposite is confirmed by Fourier transform infrared spectroscopy, Raman spectroscopy and X-ray diffraction. The field emission scanning electron microscopy images clearly showed that PPy/MnO₂ was uniformly coated on PPy|GO. The PPy|GO|PPy/MnO₂ symmetrical supercapacitor has revealed outstanding supercapacitive performance with a high specific capacitance of 786.6 F/g, an exceptionally high specific energy of 52.3 Wh/kg at a specific power of 1392.9 W/kg and preserve a good cycling stability over 1000 cycles. It is certain that PPy|GO|PPy/MnO₂ has an extraordinary perspective as an electrode for future supercapacitor developments. This finding contributes to a significant impact on the evolution of electrochemical supercapacitor.

The search and strong demand for long-lasting energy security is mainspring for the development of energy storage systems. In particular, of all energy storage systems, electrochemical supercapacitors (SCs) set its own perspectives and expectations by bridging the gap between batteries and conventional capacitors. However, certain limitations of SC need to be overcome to reinforce and instill the available technologies. An ideal SC should have larger specific energy than batteries and larger specific power than conventional capacitors. Even though SC is moving towards that direction, more advances in the material are needed to achieve that position. Specifically, an increment in specific capacitance will endow supercapacitor with enhanced specific energy¹. Thus, high specific energy can be achieved by making a device with high supercapacitive properties, which is usually achieved by materials that go through faradaic reactions. However, such materials usually suffer from poor cycling stabilities.

Up to now, conducting polymer, metal oxides/hydroxides and carbon-based materials have been the quintessential electrode materials for SC. The conducting polymer, polypyrrole (PPy) has received copious attention for its high capacitance, easy fabrication process, better thermal and chemical stability^{2,3}. As one of the most competitive carbon materials, graphene oxide (GO) is studied extensively as an electrode material for SC due to good conductivity and high surface area^{4,5}. Among the electroactive oxides, manganese oxides (MnO₂) is the most studied due to its high theoretical specific capacitance, environmental compatibilities and good mechanical stability^{6,7}.

Here, we are utilizing layer-by-layer (LBL) assembly as a promising approach to fabricate electrode material for SC. Basically, LBL is a process to build up a film with multiple layers by bringing in contact the substrate with solution alternatively⁸. There are various interactions involved in assembling LBL films such as electrostatic, hydrogen bonding, covalent bonding, hydrophobic interaction, van der Waals and so on^{9,10}. In the most recent, some works have been conducted on LBL for development of electrode material for SC such as polyaniline/GO^{11,12}, PPy|GO¹³ and poly(3,4-ethylenedioxythiophene)/ruthenium oxide¹⁴, in which the main idea is to bring

¹Department of Chemistry, Faculty of Science, Universiti Putra Malaysia, 43400, Serdang, Selangor, Malaysia.

²Functional Devices Laboratory, Institute of Advanced Technology, Universiti Putra Malaysia, 43400, Serdang, Selangor, Malaysia. Correspondence and requests for materials should be addressed to Y.S. (email: yusran@upm.edu.my)

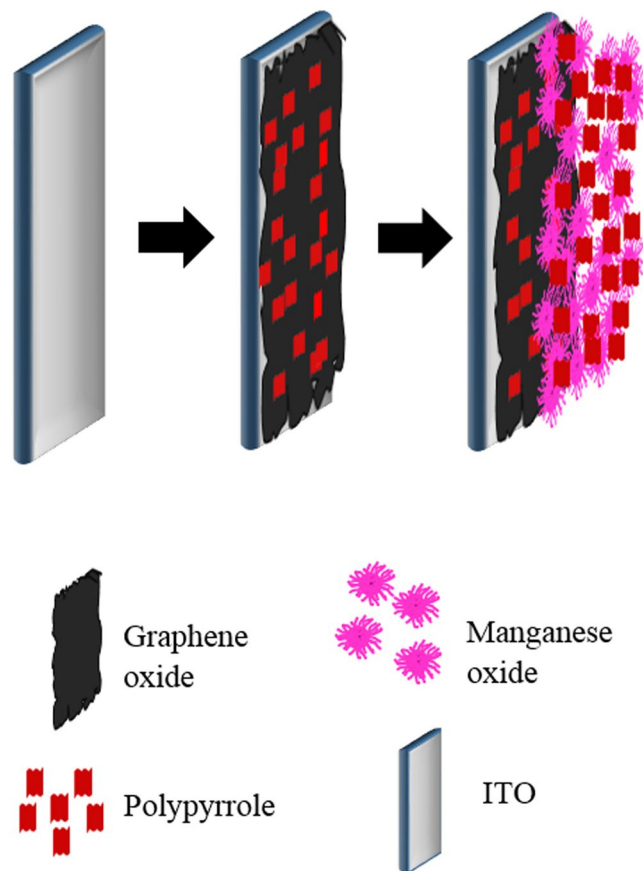


Figure 1. Schematic illustration of the preparation procedure of PPy/GO|PPy/MnO₂.

close two different material in nanoscale level. Despite all these evolvments in electrode material, the energy output of SC still subtle. Yet, the bilayer film built up of PPy/GO composite and PPy/MnO₂ composite for SC, to the best of our knowledge has never been reported.

Hence, in the current investigation, we have designed and assembled an electrode consisting of PPy/GO and PPy/MnO₂ through an LBL approach. The assembled nanocomposite has various benefits. The most anticipated virtues of this LBL assembled are (1) providing an enormous number of active sides for diffusion of electrolytes in layered composite and (2) directly forming a binder-free supercapacitor electrode on a conductive substrate, in which, it would reduce the contact resistance between electrode material and substrate. Benefiting from the synergistic effect of LBL construction, this newly designed electrode material demonstrated superior specific energy, satisfactory cycling performance and enhanced specific capacitance.

Experimental

Chemicals. Manganese sulfate monohydrate (MnSO₄·H₂O) was purchased from Sigma-Aldrich. Ethanol (95%), acetone (99.5%) and graphene oxide (GO) were supplied by HmbG Chemicals, ChemAR and Graphenea, respectively. Milli-Q deionized water (Millipore, 18.2 MΩ·cm at 25 °C) was used in all experiments. Sodium sulfate (Na₂SO₄; 99%) and pyrrole (97%; stored at 2–8 °C) were supplied by Merck. Pyrrole was distilled prior to use and other chemicals were used without any further purifications. Indium tin oxide (ITO) glasses were purchased from Xin Yan Technology Ltd.

Layer-by-layer assembly of PPy/GO with PPy/MnO₂. LBL of PPy/GO with PPy/MnO₂ (Fig. 1) was carried out by a simple and convenient electrochemical deposition method conducted using a Metrohm Autolab/M101 potentiostat. In brief, a three-electrode system was employed for electrodeposition, wherein ITO was used as a working electrode, platinum coil served as a counter electrode and silver/silver chloride (Ag/AgCl) worked as a reference electrode. Prior to the electrodeposition, the ITO substrate (geometrical area 1 cm²) was ultrasonically cleaned with ethanol, acetone and deionized water sequentially for 15 min before use. Two different solutions were prepared separately for the fabrication of LBL composite with the following procedures. 1 mg/ml GO aqueous dispersion was ultrasonicated for 60 min and was then added with 100 mM pyrrole monomer to obtain pyrrole/GO solution. Whereas, in a separate flask, 100 mM pyrrole and 0.1 M MnSO₄·H₂O was mixed in deionized water. For the preparation of LBL composite, first the PPy/GO film layer was electrodeposited on the cleaned ITO at a constant potential of 0.8 V for 10 minutes using chronoamperometry technique. After that, the PPy/MnO₂ film layer was electrodeposited on the previously obtained PPy/GO layer under the same condition. For comparison, the single layer films of PPy/GO and PPy/MnO₂ were also electrodeposited using a similar method.

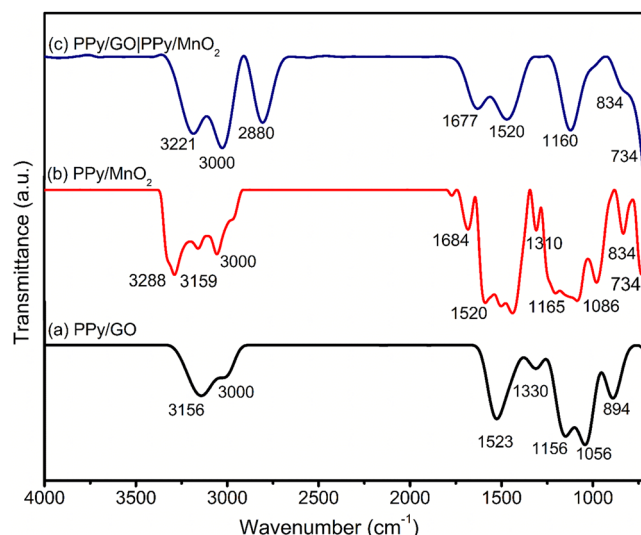


Figure 2. FTIR spectra of (a) PPy/GO, (b) PPy/MnO₂ and (c) LBL assembled composite.

Characterization. The surface morphologies of the as-prepared nanocomposites were examined by field emission scanning electron microscopy (JEOL JSM-T600F). The presence of functional groups was detected by Fourier transform infrared (FTIR, Perkin-Elmer FT-IR spectrophotometer coupled with UATR accessory) in the frequency range from 4000 to 400 cm⁻¹ and Raman spectroscopy (WITEC Alpha 300 R) in the frequency range from 4000 to 200 cm⁻¹ with an excitation wavelength of 532 nm. The X-ray diffraction (XRD) patterns were recorded with a Shimadzu X-ray diffractometer with Cu K α radiation ($\lambda = 1.54 \text{ \AA}$).

Electrochemical performance. The capacitive performance was evaluated at room temperature in a two-electrode symmetrical cell assembly, which were separated by a filter paper immersed in 1.0 M Na₂SO₄ aqueous solution. Each sample was weighed before and after electrodeposition in order to determine the mass of deposited electroactive material on ITO. The cyclic voltammetry (CV) curves, galvanostatic charge-discharge (GCD) curves, electrochemical impedance spectroscopy (EIS) plots were obtained by using a potentiostat (Metrohm Autolab/M101). The EIS measurements were performed at open circuit potential (OCP) by using a 5 mV AC sinusoid signal in the frequency range from 100 kHz to 0.01 Hz. CV measurements were carried out at the potential window between 0 to 1 V at scan rates ranging from 25 to 200 mV/s. The GCD test was performed at different current densities (3.0 to 7.0 A/g) in the potential range of 0–1 V. The specific power, specific energy and specific capacitances were measured based on the mass of both electrodes, anode and cathode. The specific capacitance was calculated from the CV curves according to the following equation:

$$C_{\text{sp}} = \frac{\int_{V_a}^{V_c} I(V) dV}{v \times m \times (V_c - V_a)} \quad (1)$$

where, C_{sp} is the specific capacitance (F/g), and V_a and V_c are the integration limits of the CV (V), I is the response current (A), v is the potential scan rate (mV/s), and m is the average mass of two electrodes (g).

The specific power and specific energy were calculated from GCD curves based on the following equations:

$$E = \frac{C_{\text{sp}} \times \Delta V^2}{2} \quad (2)$$

$$P = \frac{\Delta V \times I}{2m} \quad (3)$$

where, E is the specific energy (Wh/kg), P is the specific power (W/kg), C_{sp} is the specific capacitance (F/g), I is the discharge current (A), and ΔV is the cell operation potential (V) and m is the average mass of two electrodes (g).

Results and Discussion

Fourier Transform Infrared Spectroscopy (FTIR). The FTIR spectra of PPy/GO, PPy/MnO₂ and LBL assembled PPy/GO|PPy/MnO₂, are presented in Fig. 2. In the spectrum of PPy/GO (Fig. 2a), peaks at 3000 cm⁻¹ and 1056 cm⁻¹ are assigned to O-H and epoxide (C-O-C) of GO, respectively¹⁵. While, peaks at 3156 cm⁻¹ (N-H), 1523 cm⁻¹ (C=C stretching), 1330 cm⁻¹ (C-H plane ring deformation), 1156 cm⁻¹ (C-N plane ring) and 894 cm⁻¹ (polymerized pyrrole) are ascribed to the characteristic of PPy. However, the peak in the range of 1600–1700 cm⁻¹ that corresponding to the C=O stretching vibration of GO is disappeared due to the formation of hydrogen bond between the carboxyl groups of GO sheets and the -NH groups of PPy¹⁶. As reported by Wu *et al.*⁴, the C=C

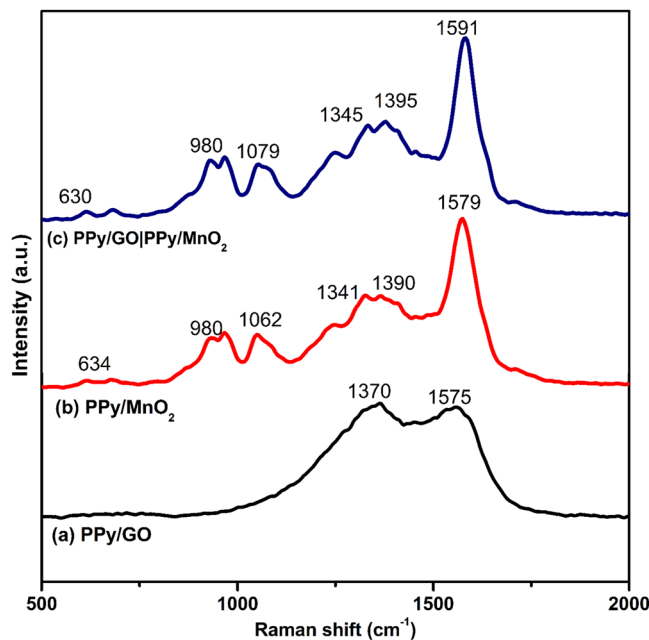


Figure 3. Raman spectra of (a) PPy/GO, (b) PPy/MnO₂ and (c) LBL assembled composite.

stretching peak of PPy is located at 1550 cm⁻¹ but this peak has shifted to 1523 cm⁻¹, indicating the existence of $\pi - \pi$ and hydrogen bonding between GO and PPy.

In the spectrum of PPy/MnO₂ (Fig. 2b), the peak around 3000 cm⁻¹ and 1684 cm⁻¹ are assigned to O-H stretching and O-H bending, respectively. Whereas, the characteristic peak of MnO₂ is noticed at 734 cm⁻¹, attributed to Mn-O bond^{17,18}. Despite this, all other main characteristic peaks of PPy are also seen in the spectrum which closely resembles peaks in the PPy/GO spectrum. However, a point to note here is that, after MnO₂ is incorporated with PPy in PPy/MnO₂, the corresponding peaks of C-N and N-H are shifted to higher frequency range compared to PPy/GO spectrum¹⁷.

The LBL assembled composite spectrum (Fig. 2c) shows the peaks approximately similar to the combination of vibration peaks of PPy/GO and PPy/MnO₂ composites. Additionally, the bands of C-O-C and C=C-N deformation are disappeared which expected that have overlapped with both of peaks of PPy at around 1060 cm⁻¹ and 834 cm⁻¹. It is noteworthy, some of the peaks in LBL assembled composite are shifted as a result of interaction between PPy/GO and PPy/MnO₂.

Raman spectroscopy. The Raman analysis for the as-synthesized nanocomposites (Fig. 3) was carried out to further confirm the presence of active materials. The existence of D and G bands in PPy/GO spectrum (Fig. 3a) are observed at 1370 cm⁻¹ and 1575 cm⁻¹, respectively. The D band is due to vibration of aromatic rings, random edges arrangement and low symmetric carbon structure¹⁹. While, the G band corresponds to the first-order scattering of the E_{2g} of sp²-bonded carbon atom^{17,20}. It is observed that the vibration bands of PPy do not appear in the range of 1350 cm⁻¹ to 1580 cm⁻¹ due to low intensity and might be overlapped with GO peaks (G and D bands). Whereas, PPy/MnO₂ (Fig. 3b) spectrum shows a peak at 634 cm⁻¹ for the Mn-O lattice vibrations. A few broad peaks at 1579 cm⁻¹ (C=C stretching), 1390 cm⁻¹ (C-N stretching), 1062 cm⁻¹ and 980 cm⁻¹ (C-H ring deformation vibration) are associated to the characteristics of PPy^{19,21}. In the spectrum of LBL assembled composite (Fig. 3c), all the characteristic peaks of PPy/MnO₂ and PPy/GO clearly appear. However, there are some peaks shifted, which could be due to electrostatic interactions and hydrogen bonding²².

X-ray diffractometry (XRD). In order to study the crystalline structure, XRD measurements were conducted on PPy/MnO₂, PPy/GO and LBL assembled PPy/GO|PPy/MnO₂, as shown in Fig. 4. The existence of MnO₂ in LBL composite was further proved by comparing the LBL composite with MnO₂ that obtained via electrodeposition under the same experimental condition. In the PPy/MnO₂ spectrum (Fig. 4a), the peaks at 26.1° (002), 37.8° (100) and 64.6° (110) are ascribed to the characteristic of MnO₂ (JCPDS No. 71-0071)²³. These diffraction peaks correspond to tetragonal MnO₂ phase. A weak and broad peak was observed in the spectra of PPy/MnO₂ (Fig. 4a) and PPy/GO (Fig. 4) at 23–35° (002) indicating the diffraction peak of PPy and further suggesting that PPy is amorphous²⁴. Moreover, the peaks for MnO₂ are intense and distinguishable, showing that a highly crystalline phase of MnO₂. Whereas, the X-ray analysis for the LBL assembled composite (Fig. 4c) shows all the characteristic peaks of PPy, GO and MnO₂, confirming the LBL composite are made up of PPy/GO and PPy/MnO₂.

Field Emission Scanning Electron Microscope (FESEM). FESEM was employed to study the morphologies of PPy/GO, PPy/MnO₂ and LBL assembled composite. The image of PPy/GO displays rough and wrinkle surface (Fig. 5a) in which the PPy particles are uniformly grown together with GO sheets by hydrogen bonding and $\pi - \pi$ interaction¹⁶. Whereas, Fig. 5b displays cauliflower like morphology indicating incorporation of MnO₂

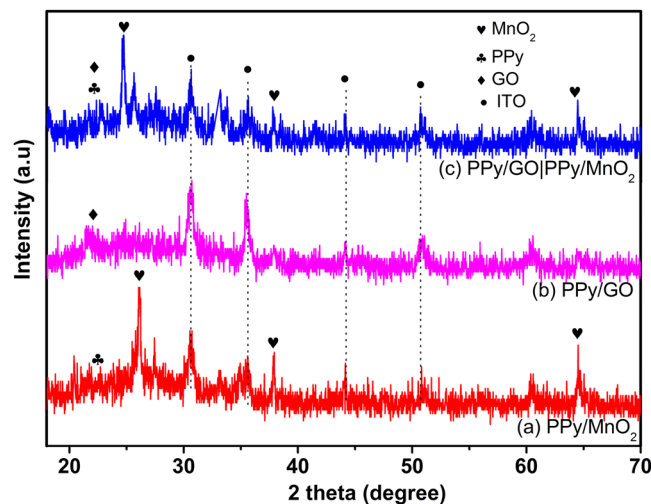


Figure 4. XRD patterns of the (a) PPy/MnO₂, (b) PPy/GO and (c) LBL assembled composites.

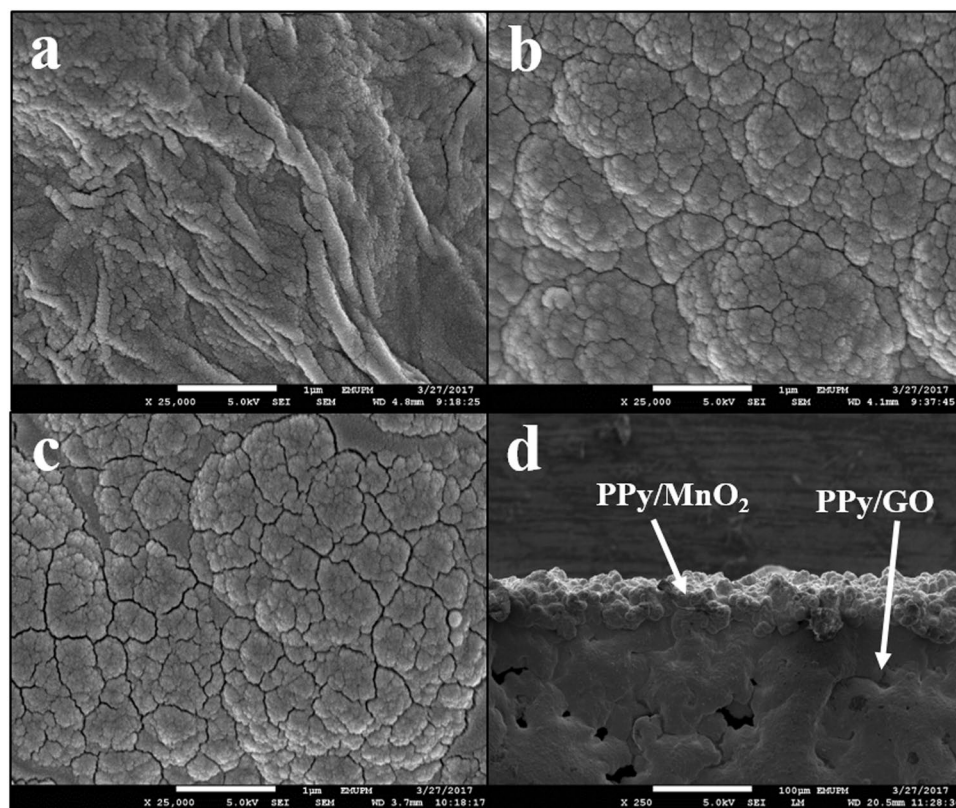


Figure 5. FESEM images of (a) PPy/GO composite, (b) PPy/MnO₂ composite and (c) LBL assembled composite and (d) cross-sectional of LBL assembled composite.

with PPy particles. This image shows a rough surface build by granular particles of composites which could provide a large surface area that enhance the performance of SC, as well as more charges can be stored. Utilizing LBL approach to electrodeposit PPy/MnO₂ onto PPy/GO forming LBL assembled PPy/GO|PPy/MnO₂ nano-composite (Fig. 5c) which has similar morphology as PPy/MnO₂ indicates PPy/MnO₂ is successfully deposited on the surface on PPy/GO. This structure allows more ion diffusion and migration in the electrodes, implying high energy capacity¹⁶. Furthermore, the existence of MnO₂ particles in the PPy matrix could increase the surface area and eventually is able to enhance the supercapacitive performance. The layered structure of LBL assembled composite can be confirmed with the cross-sectional view as shown in Fig. 5d. It is clearly seen that the film has two layers owing to PPy/GO and PPy/MnO₂.

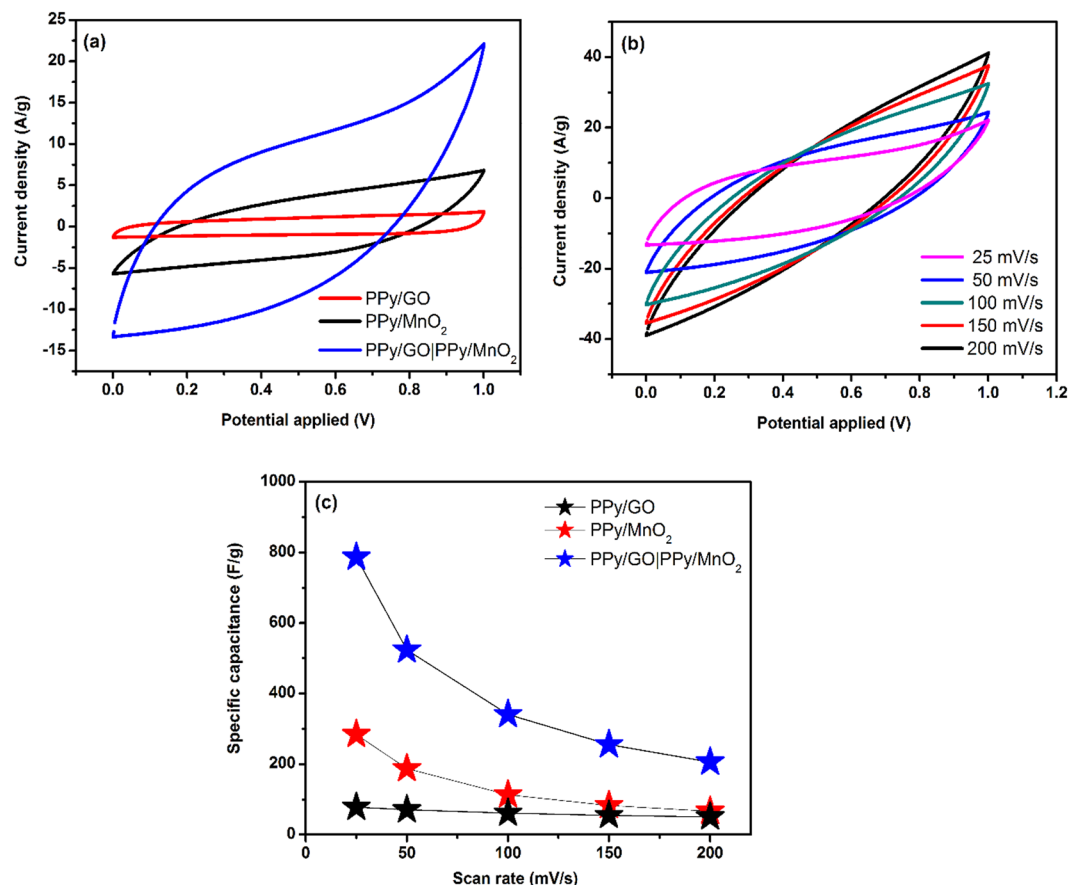


Figure 6. (a) CVs of PPy/GO, PPy/MnO₂ and LBL assembled composite at a scan rate of 25 mV/s, (b) CVs and (c) C_{sp} of LBL assembled composite at scan rate ranges from 25 to 200 mV/s.

Cyclic voltammetry. In order to investigate the electrochemical behavior of the as-prepared PPy/GO|PPy/MnO₂ composite, PPy/GO and PPy/MnO₂, cyclic voltammetric measurements were carried out using the two-electrode electrochemical system. Figure 6a shows the CV curves of LBL assembled composite, PPy/GO and PPy/MnO₂ at a scan rate of 25 mV/s in a potential range of 0 to 1 V. The CVs of LBL assembled composite and PPy/MnO₂ are quasi-rectangular, implying involvement of faradaic reaction, while the CV curves of PPy/GO is close to rectangular shape, indicating an ideal electrical double layer capacitor (EDLC) behavior²⁵. It is found that C_{sp} of LBL assembled composite (786.6 F/g) is higher than single layer composites, PPy/MnO₂ (284 F/g) and PPy/GO (78 F/g). The LBL assembled PPy/GO|PPy/MnO₂ also has a higher C_{sp} compared to the ternary GO/PPy/MnO₂ composite (207 F/g)²⁶. This indicates that LBL assembled composite provides more active sites which enhance the electrochemical performance compared to the ternary composite. As shown in Fig. 6b, the CVs of LBL assembled composite at various scan rates (25 to 200 mV/s) exhibits quasi-rectangular shapes and the CV shape remain unchanged from the lowest scan rate (25 mV/s) to the highest scan rate (200 mV/s), implying ideal SC behaviour²⁷. Moreover, the anodic and cathodic currents increase with the increasing of scan rate. However, the C_{sp} of LBL assembled bilayer composite decreases from 25 mV/s (786.6 F/g) to 200 mV/s (206 F/g) as shown in Fig. 6c due to limited ionic diffusion in the electrode material at high scan rate²⁸.

Galvanostatic charge-discharge (GCD). Figure 7a shows the GCD curves of LBL assembled composite, PPy/GO and PPy/MnO₂ at a current density of 4.0 A/g. Based on the GCD curves, PPy/MnO₂ shows asymmetry triangular shape, whereas PPy/GO has symmetrical triangular shape. Meanwhile, the large distortion of the triangular shape of LBL assembled composite is mainly due to the domination of pseudocapacitive properties in the combination of both composites²⁹. It is observed that LBL assembled composite has a longer discharging time compared to both single layer composites, indicating better capacitance behavior.

As shown in Fig. 7b, GCD curves of LBL assembled composite displays asymmetrical triangular shapes from the highest (7.0 A/g) to the lowest (3.0 A/g) current density which indicates the material has good charge-discharge reversibility³⁰. However, the discharging time decreases with the increase of current density due to the incapability of the electrolyte ions to enter into the inner structure of the active material and only the outer active surface is utilized for ion diffusion at high current densities^{16,31}. Figure 7c shows the Ragone plot (specific power vs. specific energy) of LBL assembled composite, PPy/MnO₂ and PPy/GO. The specific energy is inversely proportional to specific power. The LBL assembled shows the highest specific energy (52.35 Wh/kg) at a specific power of 1392.90 W/kg compared to

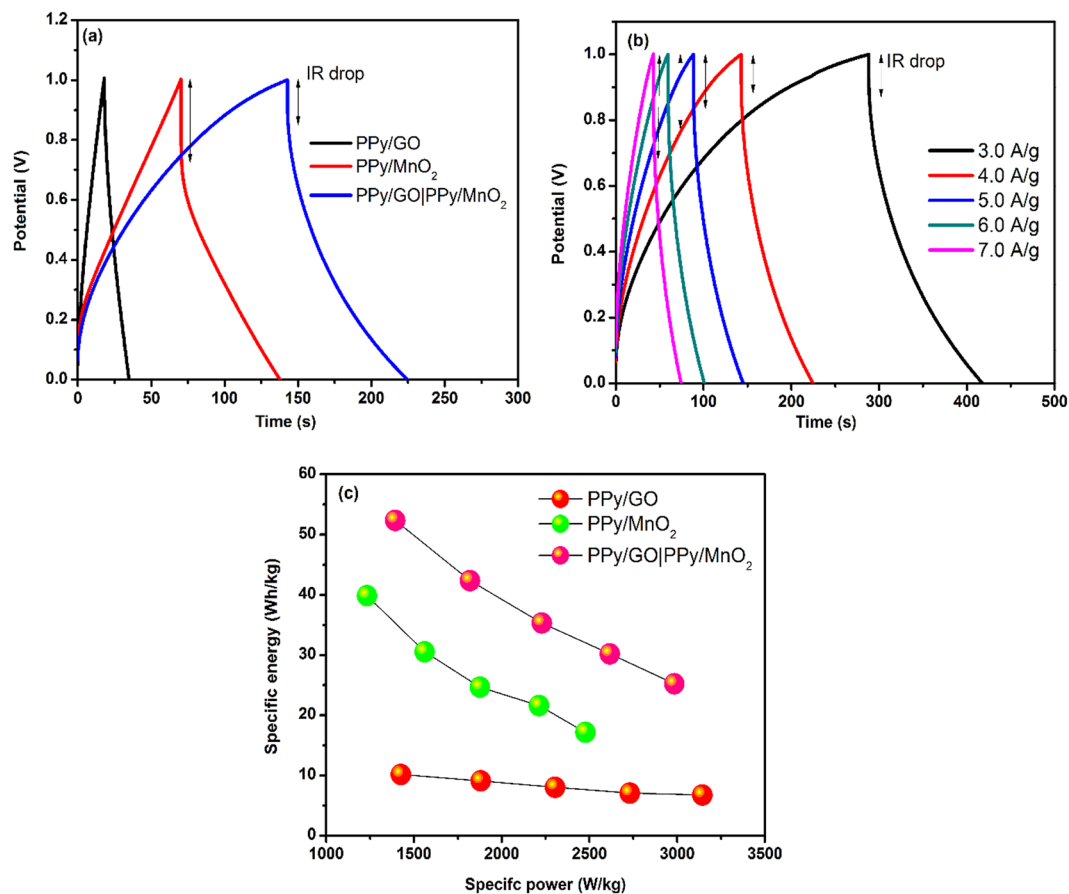


Figure 7. (a) GCD curves of LBL assembled composite, PPy/MnO₂ and PPy/GO at current density of 4.0 A/g, (b) GCD curves of LBL assembled composite at current densities of 3.0 to 7.0 A/g and (c) Ragone plot of LBL assembled composite, PPy/MnO₂ and PPy/GO composite electrodes.

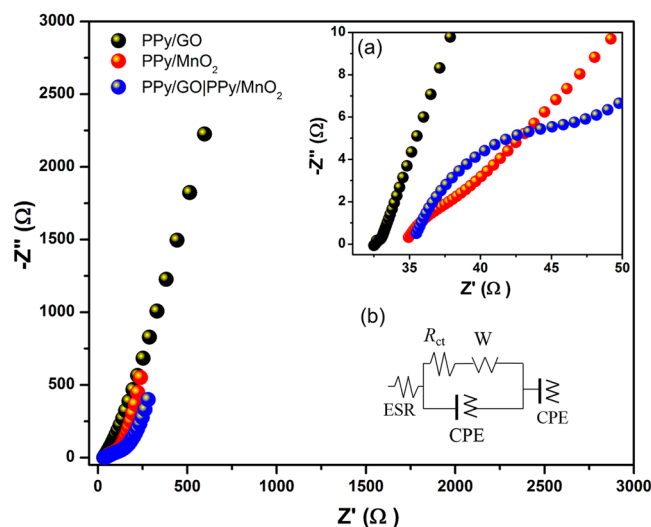


Figure 8. Nyquist plot of PPy/GO, PPy/MnO₂ and LBL assembled composite with (a) the magnified view of the Nyquist plot at high frequency and (b) equivalent circuit.

single layer composites, PPy/GO (10.12 W/kg) and PPy/MnO₂ (39.83 W/kg) at specific power of 1232.74 Wh/kg and 1425.39 Wh/kg, respectively. This indicates that properties of LBL assembled composite give significant effect in the energy performance by combining active materials of PPy/GO and PPy/MnO₂.

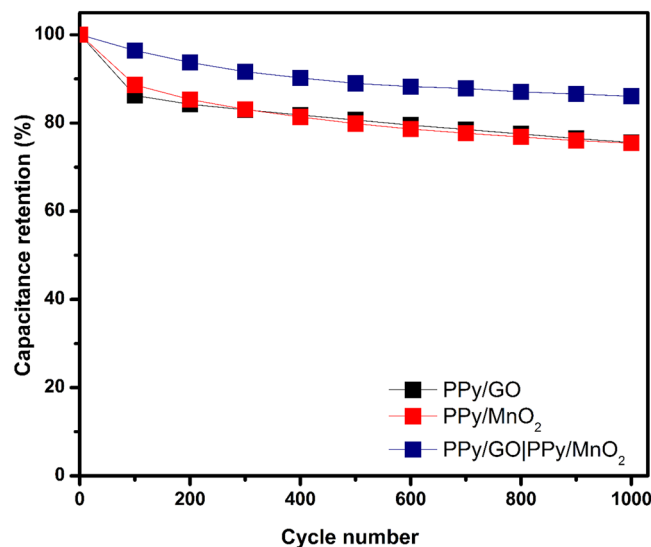


Figure 9. Specific capacitance retention of PPy/GO, PPy/MnO₂ and LBL assembled composite after 1000 cycles at a scan rate of 100 mV/s.

Material	C_{sp}	E	P	Stability	Electrolyte	Ref.
rGO/PPy	147.9 F/cm ³ at 5 A/cm ³	13.15 mWh/cm ³	1300 mW/cm ³	71.7% over 5000 cycles	PVA/H ₂ SO ₄	41
MnO ₂ /rGO	267 F/g at 0.2 A/g	17 Wh/kg	2520 W/kg	92.0% over 7000 cycles	PVA/H ₃ PO ₄	42
PPy/MnO ₂ nanotube	403 F/g at 1 A/g	—	—	88.6% over 800 cycles	1 M Na ₂ SO ₄	43
MnO ₂ /PPy/rGO	404 F/g at 0.25 A/g	—	—	91.0% over 5000 cycles	1 M Na ₂ SO ₄	17
rGO/MnO ₂ /PPy	682 F/g at 5 mV/s	—	—	86.0% over 1000 cycles	1 M Na ₂ SO ₄	44
PPy/GO PPy/MnO ₂	786.6 F/g at 25 mV/s	52.3 Wh/kg	1392.9 W/kg	86.1% over 1000 cycles	1 M Na ₂ SO ₄	This work

Table 1. Comparison of LBL assembled PPy/GO|PPy/MnO₂ with previously reported literature.

Electrochemical Impedance spectroscopy. The electrochemical performance of LBL assembled composite, PPy/GO and PPy/MnO₂ was examined by electrochemical impedance spectroscopy (EIS) which were carried out over a frequency range from 100 kHz to 0.01 Hz at open circuit potential (Fig. 8). The Nyquist plot (imaginary component ($-Z''$) versus the real component (Z')) shows the frequency response in the electrode material/electrolyte system³². All impedance spectra exhibited a vertical line approaching 90 degrees in the low frequencies region which corresponds to an ideal capacitor and fast ion diffusion in electrode materials²⁷. Based on the magnified view of the Nyquist plot (Fig. 8a), a semicircle is also observed in the high-frequency range for all impedance spectra, indicating there is a hindrance in transferring charge at the interface³³. Technically, the diameter of semicircle is associated with the charge transfer resistance (R_{ct}) and the equivalent series resistance (ESR) is obtained at the intercept point of the real-axis at high-frequency region, which is related to the electrolyte resistance, the interfacial contact resistance between current collectors and active materials and the resistance of active materials³⁴. Given in Fig. 8b, the equivalent circuit composes of ESR, R_{ct} , constant phase element (CPE) for the irregular morphologies^{35,36}, and the “classical” finite-length Warburg diffusion element (W) for the diffusion of electrolyte³⁷ is used to fit the Nyquist plot. It is clearly observed that LBL assembled composite shows a higher R_{ct} (22.62 Ω) and ESR (35.13 Ω) compared with single layers. The high ESR value is an indication of poor contact between current collector and active materials, high intrinsic resistance of active materials and high ionic resistance of electrolytes³⁸, whereas high R_{ct} value is due to the high resistance of the movement of ions at electrolyte/electrode interface³⁹ as a result of the combined resistances of both single layers.

Stability. The study on the electrochemical stability of the composites is another important parameter in evaluating the SC performance in real applications. After 1000 consecutive cycles (Fig. 9), the LBL assembled composite is able to retain exceptional cycling stability of 86.09% of its initial C_{sp} compared with both single layer composites, PPy/GO (75.58%) and PPy/MnO₂ (75.44%). These results indicate that contribution of LBL assembled PPy/GO|PPy/MnO₂ not only on promising C_{sp} , specific energy and specific power but also improves the stability of the composite which significantly decreases the destruction of electroactive materials⁴⁰ and significantly improves the stability during doping/dedoping process. The comparison with the previously published results (Table 1) indicates that our current work revealed outstanding performance and demonstrating that LBL assembled PPy/GO|PPy/MnO₂ is a promising electrode in enhancing the performance of supercapacitor.

Conclusion

LBL assembled PPy/GO|PPy/MnO₂ was successfully prepared via a simple electrodeposition approach and used as electrode material for supercapacitor with a significant improvement of performance. The uniform thin film showed a high specific capacitance of 786.6 F/g at 25 mV/s, with the high specific energy of 53.3 Wh/kg at a specific power of 1392.9 W/kg, which are promising values for a high-performance supercapacitor. PPy/GO|PPy/MnO₂ composite gained the advantage of LBL assembly, is apt to be an electrode for supercapacitor.

References

- Demarconnay, L., Raymundo-Piñero, E. & Béguin, F. Adjustment of electrodes potential window in an asymmetric carbon/MnO₂ supercapacitor. *J. Power Sources* **196**, 580–586, <https://doi.org/10.1016/j.jpowsour.2010.06.013> (2011).
- Wei, H. *et al.* Electropolymerized polypyrrole nanocomposites with cobalt oxide coated on carbon paper for electrochemical energy storage. *Polymer* **67**, 192–199, <https://doi.org/10.1016/j.polymer.2015.04.064> (2015).
- Chen, J. *et al.* Facile Co-Electrodeposition Method for High-Performance Supercapacitor Based on Reduced Graphene Oxide/Polypyrrole Composite Film. *ACS Appl. Mater. Interfaces* **9**, 19831–19842, <https://doi.org/10.1021/acsami.7b03786> (2017).
- Wu, W. *et al.* Core-shell nanospherical polypyrrole/graphene oxide composites for high performance supercapacitors. *RSV Adv.* **5**, 91645–91653, <https://doi.org/10.1039/c5ra17036b> (2015).
- Dreyer, D. R., Park, S., Bielawski, C. W. & Ruoff, R. S. The chemistry of graphene oxide. *Chemical Society Reviews* **39**, 228–240, <https://doi.org/10.1039/B917103G> (2010).
- Zhu, S. *et al.* Structural directed growth of ultrathin parallel birnessite on β -MnO₂ for high-performance asymmetric supercapacitors. *ACS Nano* **12**, 1033–1042, <https://doi.org/10.1021/acsnano.7b03431> (2018).
- Khan, M. *et al.* Graphene based metal and metal oxide nanocomposites: synthesis, properties and their applications. *J. Mater. Chem A* **3**, 18753–18808, <https://doi.org/10.1039/C5TA02240A> (2015).
- Kulandaivalu, S., Abdul Shukur, R. & Sulaiman, Y. Improved electrochemical performance of electrochemically designed layered poly(3,4-ethylenedioxythiophene)/graphene oxide with poly(3,4-ethylenedioxythiophene)/nanocrystalline cellulose nanocomposite. *Synth. Met* **245**, 24–31, <https://doi.org/10.1016/j.synthmet.2018.08.002> (2018).
- Zhu, J. & He, J. Assembly and benign step-by-step post-treatment of oppositely charged reduced graphene oxides for transparent conductive thin films with multiple applications. *Nanoscale* **4**, 3558–3566, <https://doi.org/10.1039/C2NR30606A> (2012).
- Wang, L. *et al.* A new approach for the fabrication of an alternating multilayer film of poly(4-vinylpyridine) and poly(acrylic acid) based on hydrogen bonding. *Macromolecular Rapid Communications* **18**, 509–514, <https://doi.org/10.1002/marc.1997.030180609> (1997).
- Mitchell, E. *et al.* High performance supercapacitor based on multilayer of polyaniline and graphene oxide. *Synth. Met* **199**, 214–218, <https://doi.org/10.1016/j.synthmet.2014.11.028> (2015).
- Lee, T. *et al.* Hybrid multilayer thin film supercapacitor of graphene nanosheets with polyaniline: importance of establishing intimate electronic contact through nanoscale blending. *J. Mater. Chem* **22**, 21092–21099, <https://doi.org/10.1039/C2JM33111J> (2012).
- Zhang, L. L., Zhao, S., Tian, X. N. & Zhao, X. S. Layered graphene oxide nanostructures with sandwiched conducting polymers as supercapacitor electrodes. *Langmuir* **26**, 17624–17628, <https://doi.org/10.1021/la103413s> (2010).
- Hong, J.-I., Yeo, I.-H. & Paik, W.-K. Conducting polymer with metal oxide for electrochemical capacitor: poly(3,4-ethylenedioxythiophene) RuO_x electrode. *Journal of The Electrochemical Society* **148**, A156–A163, <https://doi.org/10.1149/1.1342166> (2001).
- De la Fuente Salas, I. M., Sudhakar, Y. N. & Selvakumar, M. High performance of symmetrical supercapacitor based on multilayer films of graphene oxide/polypyrrole electrodes. *Applied Surface Science* **296**, 195–203, <https://doi.org/10.1016/j.apsusc.2014.01.080> (2014).
- Fan, L.-Q. *et al.* Asymmetric supercapacitor based on graphene oxide/polypyrrole composite and activated carbon electrodes. *Electrochim. Acta* **137**, 26–33, <https://doi.org/10.1016/j.electacta.2014.05.137> (2014).
- Han, G. *et al.* Sandwich-structured MnO₂/polypyrrole/reduced graphene oxide hybrid composites for high-performance supercapacitors. *RSC Adv.* **4**, 9898, <https://doi.org/10.1039/c3ra47764a> (2014).
- Yuan, L., Wan, C. & Zhao, L. Facial *in-situ* synthesis of MnO₂/PPy composite for supercapacitor. *International Journal of Electrochemical Science* **10**, 9456–9465 (2015).
- Fan, X., Yang, Z. & He, N. Hierarchical nanostructured polypyrrole/graphene composites as supercapacitor electrode. *RSV Adv.* **5**, 15096–15102, <https://doi.org/10.1039/c4ra15258a> (2015).
- Mohd Abdah, M. A. A., Zubair, N. A., Azman, N. H. N. & Sulaiman, Y. Fabrication of PEDOT coated PVA-GO nanofiber for supercapacitor. *Materials Chemistry and Physics* **192**, 161–169, <https://doi.org/10.1016/j.matchemphys.2017.01.058> (2017).
- Du, H., Xie, Y., Xia, C., Wang, W. & Tian, F. Electrochemical capacitance of polypyrrole–titanium nitride and polypyrrole–titanium nanotube hybrids. *New Journal of Chemistry* **38**, 1284, <https://doi.org/10.1039/c3nj01286g> (2014).
- Wang, H., Bian, L., Zhou, P., Tang, J. & Tang, W. Core-sheath structured bacterial cellulose/polypyrrole nanocomposites with excellent conductivity as supercapacitors. *J. Mater. Chem A* **1**, 578–584, <https://doi.org/10.1039/C2TA00040G> (2013).
- Sivakkumar, S. R., Ko, J. M., Kim, D. Y., Kim, B. C. & Wallace, G. G. Performance evaluation of CNT/polypyrrole/MnO₂ composite electrodes for electrochemical capacitors. *Electrochim. Acta* **52**, 7377–7385, <https://doi.org/10.1016/j.electacta.2007.06.023> (2007).
- Zhou, H., Han, G., Xiao, Y., Chang, Y. & Zhai, H.-J. Facile preparation of polypyrrole/graphene oxide nanocomposites with large areal capacitance using electrochemical codeposition for supercapacitors. *J. Power Sources* **263**, 259–267 (2014).
- Chang, H.-H., Chang, C.-K., Tsai, Y.-C. & Liao, C.-S. Electrochemically synthesized graphene/polypyrrole composites and their use in supercapacitor. *Carbon* **50**, 2331–2336, <https://doi.org/10.1016/j.carbon.2012.01.056> (2012).
- Ji, J. *et al.* One-step synthesis of graphene oxide/polypyrrole/MnO₂ ternary nanocomposites with an improved electrochemical capacitance. *Journal of Nanoscience and Nanotechnology* **17**, 4356–4361, <https://doi.org/10.1166/jnn.2017.13097> (2017).
- Khoh, W.-H. & Hong, J.-D. Layer-by-layer self-assembly of ultrathin multilayer films composed of magnetite/reduced graphene oxide bilayers for supercapacitor application. *Colloids and Surfaces A: Physicochemical and Engineering Aspects* **436**, 104–112, <https://doi.org/10.1016/j.colsurfa.2013.06.012> (2013).
- Sharma, R. K., Rastogi, A. C. & Desu, S. B. Manganese oxide embedded polypyrrole nanocomposites for electrochemical supercapacitor. *Electrochim. Acta* **53**, 7690–7695, <https://doi.org/10.1016/j.electacta.2008.04.028> (2008).
- Wang, X. *et al.* Layer-by-layer assembled hybrid multilayer thin film electrodes based on transparent cellulose nanofibers paper for flexible supercapacitors applications. *J. Power Sources* **249**, 148–155, <https://doi.org/10.1016/j.jpowsour.2013.09.130> (2014).
- Lu, L., Xu, S., An, J. & Yan, S. Electrochemical performance of CNTs/RGO/MnO₂ composite material for supercapacitor. *Nanomaterials and Nanotechnology* **6**, 184798041666368, <https://doi.org/10.1177/1847980416663687> (2016).
- Jiang, D. B., Zhang, B. Y., Zheng, T. X., Zhang, Y. X. & Xu, X. One-pot synthesis of η -Fe₂O₃ nanospheres/diatomite composites for electrochemical capacitor electrodes. *Materials Letters* **215**, 23–26, <https://doi.org/10.1016/j.matlet.2017.12.059> (2018).
- Sarker, A. K. & Hong, J. D. Layer-by-layer self-assembled multilayer films composed of graphene/polyaniline bilayers: high-energy electrode materials for supercapacitors. *Langmuir* **28**, 12637–12646, <https://doi.org/10.1021/la3021589> (2012).

33. Wu, J. *et al.* Three-dimensional hierarchical interwoven nitrogen-doped carbon nanotubes/Co₂Ni_{1-x}-layered double hydroxides ultrathin nanosheets for high-performance supercapacitors. *Electrochim. Acta* **203**, 21–29, <https://doi.org/10.1016/j.electacta.2016.04.033> (2016).
34. Luo, J., Ma, Q., Gu, H., Zheng, Y. & Liu, X. Three-dimensional graphene-polyaniline hybrid hollow spheres by layer-by-layer assembly for application in supercapacitor. *Electrochim. Acta* **173**, 184–192 (2015).
35. Zubair, N. A., Rahman, N. A., Lim, H. N., Zawawi, R. M. & Sulaiman, Y. Electrochemical properties of PVA-GO/PEDOT nanofibers prepared using electrospinning and electropolymerization techniques. *RSC Adv.* **6**, 17720–17727, <https://doi.org/10.1039/C5RA21230H> (2016).
36. Lai, L. *et al.* Preparation of supercapacitor electrodes through selection of graphene surface functionalities. *ACS Nano* **6**, 5941–5951, <https://doi.org/10.1021/nn3008096> (2012).
37. Taberna, P.-L. & Simon, P. In *Supercapacitors: Materials, Systems and Applications* (eds F. Béguin & E. Frąckowiak) Ch. 3, 111–130 (Wiley-VCH Verlag GmbH & Co. KGaA, 2013).
38. Zhu, S. J. *et al.* Rational design of octahedron and nanowire CeO₂@MnO₂ core-shell heterostructures with outstanding rate capability for asymmetric supercapacitors. *Chemical Communications* **51**, 14840–14843, <https://doi.org/10.1039/C5CC03976B> (2015).
39. Meher, S. K. & Rao, G. R. Ultralayered Co₃O₄ for high-performance supercapacitor applications. *The Journal of Physical Chemistry C* **115**, 15646–15654, <https://doi.org/10.1021/jp201200e> (2011).
40. Zhu, C., Zhai, J., Wen, D. & Dong, S. Graphene oxide/polypyrrole nanocomposites: one-step electrochemical doping, coating and synergistic effect for energy storage. *J. Mater. Chem* **22**, 6300, <https://doi.org/10.1039/c2jm16699b> (2012).
41. Liu, X. *et al.* Preparation of on chip, flexible supercapacitor with high performance based on electrophoretic deposition of reduced graphene oxide/polypyrrole composites. *Carbon* **92**, 348–353, <https://doi.org/10.1016/j.carbon.2015.05.039> (2015).
42. Peng, L. *et al.* Ultrathin two-dimensional MnO₂/graphene hybrid nanostructures for high-performance, flexible planar supercapacitors. *Nano Letters* **13**, 2151–2157, <https://doi.org/10.1021/nl400600x> (2013).
43. Ji, J. *et al.* Assembly of polypyrrole nanotube@MnO₂ composites with an improved electrochemical capacitance. *Materials Science and Engineering: B* **198**, 51–56, <https://doi.org/10.1016/j.mseb.2015.04.004> (2015).
44. Zhou, H. *et al.* RGO/MnO₂/polypyrrole ternary film electrode for supercapacitor. *Materials Chemistry and Physics* **177**, 40–47, <https://doi.org/10.1016/j.matchemphys.2016.03.035> (2016).

Acknowledgements

This work was supported by Universiti Putra Malaysia Grant (GP-IPS/2017/9580500).

Author Contributions

Y.S. supervised and coordinated the whole experiments. S.K. and N.S. performed the experiments, carried out the measurements, data analysis, reporting results and data interpretation. S.K. wrote the main manuscript.

Additional Information

Competing Interests: The authors declare no competing interests.

Publisher's note: Springer Nature remains neutral with regard to jurisdictional claims in published maps and institutional affiliations.



Open Access This article is licensed under a Creative Commons Attribution 4.0 International License, which permits use, sharing, adaptation, distribution and reproduction in any medium or format, as long as you give appropriate credit to the original author(s) and the source, provide a link to the Creative Commons license, and indicate if changes were made. The images or other third party material in this article are included in the article's Creative Commons license, unless indicated otherwise in a credit line to the material. If material is not included in the article's Creative Commons license and your intended use is not permitted by statutory regulation or exceeds the permitted use, you will need to obtain permission directly from the copyright holder. To view a copy of this license, visit <http://creativecommons.org/licenses/by/4.0/>.

© The Author(s) 2019